

Effects of Pressure on the Electronic and Magnetic Properties of Bulk NiI₂

Jesse Kapeghian,^{1,*} Danila Amoroso,² Connor A. Occhialini,³ Luiz G. P. Martins,³
Qian Song,³ Jesse S. Smith,⁴ Joshua J. Sanchez,³ Jing Kong,⁵ Riccardo Comin,³
Paolo Barone,⁶ Bertrand Dupé,^{2,7} Matthieu J. Verstraete,^{2,8} and Antia S. Botana^{1,†}

¹*Department of Physics, Arizona State University, Tempe, AZ - 85287, USA*

²*Nanomaterials/Quantum Materials/CESAM, Université de Liège, B-4000 Sart Tilman, Belgium*

³*Department of Physics, Massachusetts Institute of Technology, Cambridge, MA 02139, USA*

⁴*HPCAT, Advanced Photon Source, Argonne National Laboratory, Lemont, IL 60439, USA*

⁵*Department of Electrical Engineering and Computer Science,
Massachusetts Institute of Technology, Cambridge, MA 02139, USA*

⁶*Consiglio Nazionale delle Ricerche CNR-SPIN, Area della Ricerca di Tor Vergata,
Via del Fosso del Cavaliere 100, I-00133 Rome, Italy*

⁷*Fonds de la Recherche Scientifique (FNRS), Bruxelles, Belgium*

⁸*European Theoretical Spectroscopy Facility www.etsf.eu*

(Dated: June 9, 2023)

Transition metal dihalides have recently garnered interest in the context of two-dimensional van der Waals magnets as their underlying geometrically frustrated triangular lattice leads to interesting competing exchange interactions. In particular, NiI₂ is a magnetic semiconductor that has been long known for its exotic helimagnetism in the bulk. Recent experiments have shown that the helimagnetic state survives down to the monolayer limit with a layer-dependent magnetic transition temperature that suggests a relevant role of the interlayer coupling. Here, we explore the effects of hydrostatic pressure as a means to enhance this interlayer exchange and ultimately tune the electronic and magnetic response of NiI₂. We study first the evolution of the structural parameters as a function of external pressure using first-principles calculations combined with x-ray diffraction measurements. We then examine the evolution of the electronic structure and magnetic exchange interactions via first-principles calculations and Monte Carlo simulations. We find that the leading interlayer coupling is an antiferromagnetic second-nearest neighbor interaction that increases monotonically with pressure. The ratio between isotropic third- and first-nearest neighbor intralayer exchanges, which controls the magnetic frustration and determines the magnetic propagation vector \mathbf{q} of the helimagnetic ground state, is also enhanced by pressure. As a consequence, our Monte Carlo simulations show a monotonic increase in the magnetic transition temperature, indicating that pressure is an effective means to tune the magnetic response of NiI₂.

I. INTRODUCTION

Magnetic two dimensional (2D) van der Waals (vdW) materials have attracted much attention¹ since Ising-type magnetic orders were demonstrated in the monolayer limit for antiferromagnetic FePS₃^{2,3} and for ferromagnetic CrI₃⁴. This series of discoveries naturally led researchers to explore the possibility of realizing both electric and magnetic orders simultaneously in a vdW material down to the single-layer limit. In this context, transition metal (TM) dihalides are emerging as novel platforms to explore magnetoelectricity and noncollinear spin textures in 2D. Indeed, recent experiments⁵ in NiI₂ have revealed that multiferroicity (MF) in this compound persists from the bulk to the monolayer limit leading to the realization of a vdW material that simultaneously displays magnetic and ferroelectric order.

Structurally, bulk NiI₂ adopts the rhombohedral ($R\bar{3}m$) CdCl₂ crystal lattice at room temperature, containing triangular nets of TM (Ni) cations in edge sharing octahedral coordination and forming NiI₂ layers separated by vdW gaps⁶⁻⁸ (see Fig. 1). Bulk NiI₂ is known to undergo two phase transitions upon cooling; the first is to an antiferromagnetic (AFM) state with a Néel temperature $T_{N,1} \simeq 75$ K and the second transition is to a

single- \mathbf{q} proper-screw helimagnetic (HM) ground state at $T_{N,2} \simeq 60$ K⁸⁻¹³. The $T_{N,2}$ transition is concomitant with a lowering of the crystal symmetry from rhombohedral to monoclinic^{13,14}. In addition, $T_{N,2}$ also marks the onset of type-II MF order^{5,15} as it was found that the non-collinear magnetic state hosts a ferroelectric polarization tunable via a magnetic field. As mentioned above, the HM state in NiI₂ is found to be robust down to the single-layer limit with experiments indicating that $T_{N,2}$ decreases monotonically with the number of layers⁵. This continuous decrease of $T_{N,2}$ indicates that the interlayer exchange coupling plays an important role in the magnetic order of NiI₂⁵.

Exploring ways to enhance the interlayer exchange in NiI₂, in order to tune its electronic and magnetic response, is then a natural path to pursue. Here, we study the effects of hydrostatic pressure as a means to achieve this goal, using first-principles calculations in conjunction with high-pressure x-ray diffraction (XRD) experiments. We present a systematic density-functional theory (DFT)-based study of the magnetic interactions of NiI₂ under pressures up to 20 GPa. We find that pressure has a significant effect on the interlayer coupling, but also in some of the leading intralayer interactions. Specifically, while the dominant intralayer exchange at ambient pressure (ferromagnetic

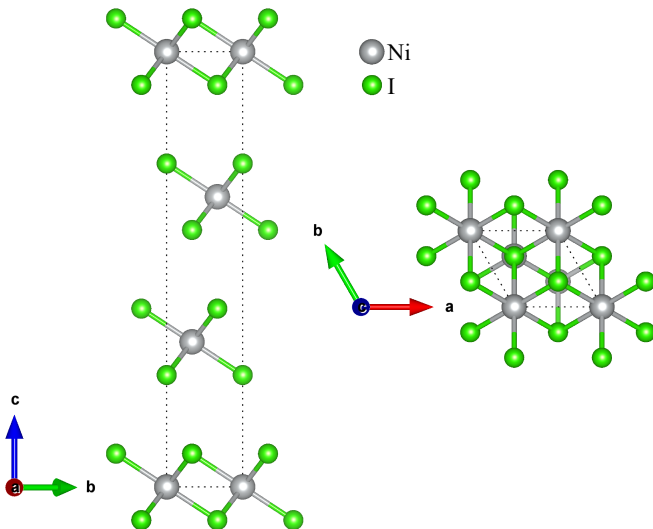


FIG. 1. Crystal structure of bulk NiI_2 in the rhombohedral ($R\bar{3}m$) phase showing the out-of-plane (left) and in-plane (right) arrangement of atoms, where gray (green) spheres represent Ni (I) atoms and the unit cell boundary is marked by a black dotted line.

nearest-neighbor $J^{\parallel 1}$) is weakly pressure dependent, there is a significant enhancement of the antiferromagnetic third nearest-neighbor intralayer interaction ($J^{\parallel 3}$) and of the antiferromagnetic interlayer exchange ($J^{\perp \text{eff}}$). Monte Carlo (MC) simulations reveal a 3-fold increase in the helimagnetic transition temperature between 0 and 10 GPa followed by saturation at higher pressures.

II. COMPUTATIONAL METHODS

A. First-Principles Calculations

We performed DFT-based calculations using the projector augmented wave (PAW) method¹⁶ as implemented in the VASP code^{17,18}. The wave functions were expanded in the plane-wave basis with a kinetic-energy cut-off of 500 eV. Consistent with our previous work (see Refs. [5 and 19]), the $3p$, $3d$, and $4s$ orbitals ($3p^6 3d^9 4s^1$ configuration) were considered as valence states for the Ni atoms while for the I atoms the $5s$ and $5p$ orbitals ($5s^2 5p^5$ configuration) were as considered valence states.

Hydrostatic pressure was applied in increments of 5 GPa during relaxation for pressures up to 20 GPa. The structural degrees of freedom considered during the optimization of the bulk unit cells at each pressure were atomic positions, cell shape, and cell volume, and we restricted our analysis to the rhombohedral phase. Tolerances for energy and force minimization during relaxation were set at 10^{-10} eV and 10^{-3} eV/Å, respectively. Different DFT functionals and spin configurations were tested, after which the structural parameters were compared to those obtained from experimental XRD data. The best

agreement was obtained for an AFM state (consisting ferromagnetic (FM) planes coupled AFM out-of-plane) using the Perdew-Burke-Ernzerhof (PBE)²⁰ version of the generalized gradient approximation (GGA) functional with the DFT-D3 van der Waals correction²¹, and including an on-site Coulomb repulsion U using the Liechtenstein²² approach in order to account for correlation effects in the Ni- d electrons²³. The U and Hund's coupling J_H values used (3.24 and 0.68 eV, respectively) were taken from constrained random phase approximation (cRPA) calculations²⁴. To accommodate the AFM order, a $1 \times 1 \times 2$ supercell was used and the sampling over the Brillouin zone (BZ) was performed with a $36 \times 36 \times 3$ Monkhorst-Pack k -mesh centered on Γ . Note that this AFM order is consistent with the c -component of the magnetic propagation vector, that is $\sim 3/2$ not only for NiI_2 but across the Ni-dihalide series⁸. Electronic structure calculations for the optimized bulk structures at each pressure were performed with a tolerance of 10^{-8} eV for the electronic energy minimization.

Consistently with Ref. [19], we employed the four-state method (explained in detail in Refs. [25–29]) to calculate the exchange couplings and anisotropies for NiI_2 . The four-state method is based on total energy mapping through noncollinear, magnetic DFT calculations, including spin-orbit coupling (SOC). Each magnetic interaction parameter is related to the energies of four distinct magnetic configurations wherein the directions of the magnetic moments were constrained and large supercells were used to inhibit coupling between distant neighbors. At each pressure, intralayer (interlayer) magnetic constants were calculated using monolayer (bilayer) structures built from the relaxed bulk structures. In both the mono- and bilayers, we used a distance of more than 20 Å with respect to the periodic repetition along the out-of-plane direction. For the monolayers, a $5 \times 4 \times 1$ supercell was used for first- and second-nearest in-plane neighbors (and single-ion anisotropy) and a $6 \times 3 \times 1$ supercell was used for third-nearest in-plane neighbors. For the bilayer, a $3 \times 3 \times 1$ supercell was used for first-, second-, and third-nearest out-of-plane neighbors. In all mono- and bilayer cases, a Γ -centered $6 \times 6 \times 2$ k -mesh was employed for BZ sampling.

B. Monte Carlo Simulations

We used the simulation code Matjes³⁰ to perform Monte Carlo calculations and extract the critical temperatures. Specifically, up to $\sim 10^6$ thermalization steps were used at each simulated temperature followed by 10^4 MC steps for statistical averaging. At each temperature, the average total energy, magnetization, and specific heat were calculated. Further, a standard Metropolis algorithm was used on supercells of size $L \times L \times 4$ with periodic boundary conditions. For each bulk structure optimized at a different pressure, the supercell size L was chosen according to $L \simeq nL_{\text{m.u.c.}}$ where n is an integer and $L_{\text{m.u.c.}}$ is

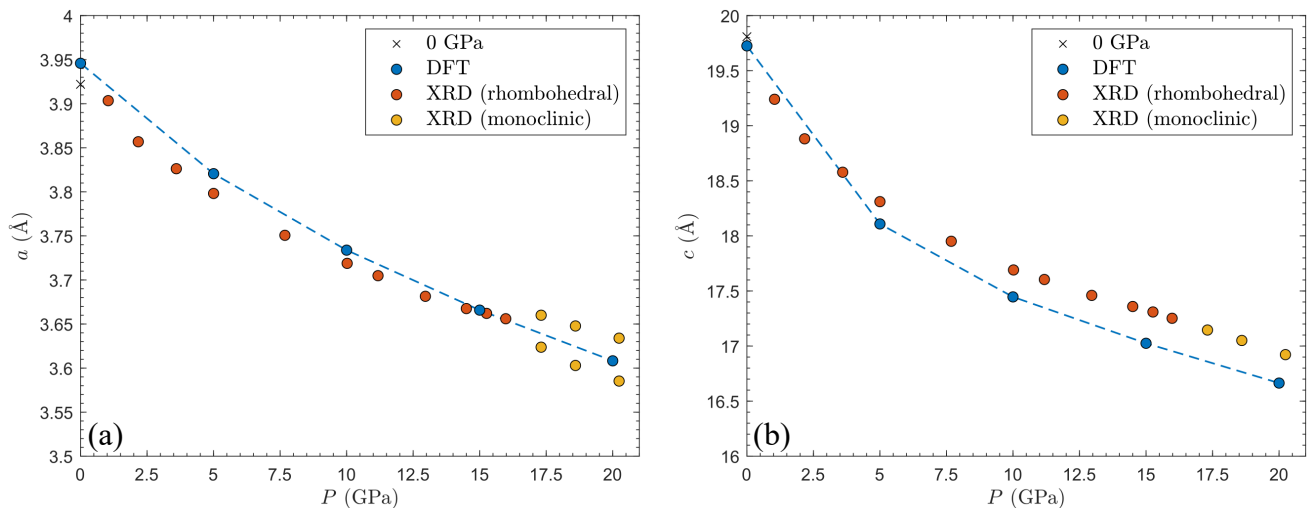


FIG. 2. In-plane (a) and out-of-plane (b) relaxed lattice parameters for bulk NiI_2 from DFT (blue circles) along with our experimental XRD data (orange/yellow circles for rhombohedral/monoclinic phases) taken at various pressures at 200 K. The black crosses represent ambient pressure experimental values obtained from neutron diffraction experiments at 300 K: $a = 3.922$ Å, $c = 19.808$ Å¹³.

the minimum lateral size of the magnetic unit cell which is required to faithfully represent the noncollinear spin configuration of the HM ground state. The magnetic unit cell length can be estimated as $L_{\text{m.u.c.}} \sim 4\pi/q$, where q is the magnitude of the magnetic propagation vector \mathbf{q} which minimizes the exchange interaction energy in momentum space. Considering an isotropic model where the second nearest-neighbor interaction is neglected, an analytical solution can be obtained for the wave vector, $q = 2 \arccos \left[\left(1 + \sqrt{1 - 2(J^{\parallel 1}/J^{\parallel 3})} \right) / 4 \right]$ ^{31,32}.

III. RESULTS

A. Structural Optimizations and Electronic Structure

Fig. 2 shows the optimized bulk lattice parameters calculated at pressures up to 20 GPa via first-principles calculations. These lattice parameters were derived within an AFM state (consisting of FM planes coupled AFM out-of-plane) using the GGA-PBE functional including a DFT-D3 correction and an on-site Coulomb repulsion $U = 3.24$ eV. Computational results are compared with experimental values in the same pressure range. The ambient pressure experimental structural data are taken from Ref. [13] (at 300 K) while for finite pressures the data are obtained from our XRD experiments performed at 200 K (see Appendix A for further details). Up to ~ 15 GPa the experimental in-plane lattice parameters (orange circles) are equivalent indicating rhombohedral symmetry (i.e. $a = b$), while above ~ 15 GPa there is a splitting in the in-plane lattice parameter (yellow circles) indicating a symmetry-lowering to a monoclinic phase ($a \neq b$). DFT

calculations are restricted to the rhombohedral phase, as explained above. The DFT-derived optimized lattice parameters show in-plane lattice constants ($a = b$) that exhibit a monotonic decrease with increasing pressure (from ~ 3.95 Å at ambient pressure to ~ 3.61 Å at 20 GPa), in good agreement with the experimental data (Fig. 2a). An expected monotonic decrease is also observed in the out-of-plane optimized lattice parameter (c) with increasing pressure (from ~ 19.72 Å at ambient pressure to ~ 16.66 Å at 20 GPa) with the experimental data showing the same trends (Fig. 2b). As expected for a vdW material, the structural response of NiI_2 to pressure is highly anisotropic with the c lattice parameter showing a rate of compression that is roughly double that of the a lattice parameter. For additional optimization calculations using various computational methods, see Appendix A.

Fig. 3 shows the evolution of the corresponding band structure of NiI_2 upon pressure for the optimized structures described above (at 0, 15, and 20 GPa). The insulator-to-metal transition can be clearly observed: an insulating solution is obtained up to 15 GPa and a metallic state at 20 GPa, consistent with the experimentally reported insulator-to-metal transition at 19 GPa³³ (see Appendix B for a full evolution of the band structure from 0-20 GPa). Note that along the Γ to A directions some bands are quite dispersive indicating a relatively large degree of interaction between layers. This out-of-plane dispersion increases with pressure: that is, as the interlayer distance decreases. Orbital-resolved densities of states (DOS) along with band character plots indicate that the dispersion is driven primarily from the $I-p_z$ states (see Appendix B).

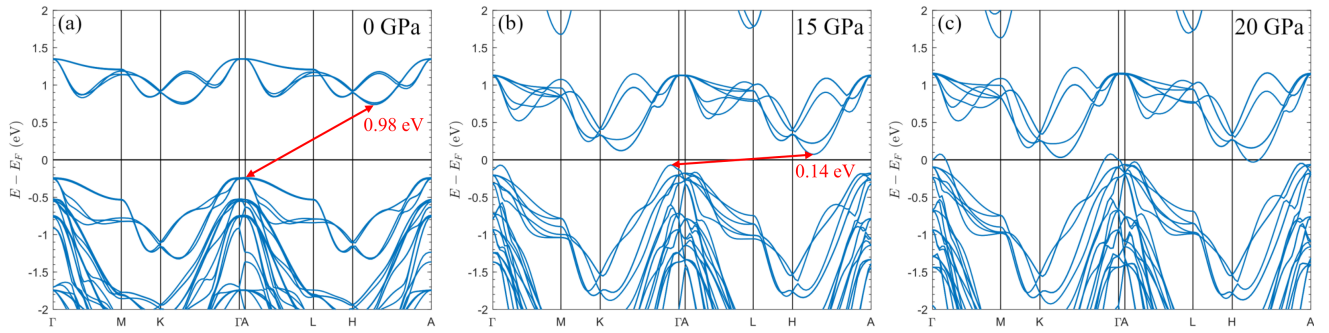


FIG. 3. GGA-PBE+D3+U (3.24 eV) band structure plots for bulk Ni₂ (calculated with AFM order) at ambient pressure (a), 15 GPa (b) and 20 GPa (c) where the energy band gaps are indicated in both cases. Reciprocal space coordinates: $\Gamma = (0, 0, 0)$, $M = (1/2, 0, 0)$, $K = (1/3, 1/3, 0)$, $A = (0, 0, 1/2)$, $L = (1/2, 0, 1/2)$, $H = (1/3, 1/3, 1/2)$ (see Appendix B for the schematic of the BZ showing these high-symmetry points).

B. Exchange Interactions

The relevant magnetic interactions between localized spins (\mathbf{S}_i) in Ni₂ are the intra- and interlayer exchange couplings and the single-ion anisotropy. The microscopic model which encapsulates the in-plane interactions is given by the 2D anisotropic Heisenberg Hamiltonian used in Ref. [19] to describe monolayer Ni₂, to which we have added an isotropic interlayer exchange term to account for the magnetic interactions between layers (we only consider the isotropic component for the out-of-plane exchange since the short-range anisotropic contributions arising from the spin-orbit interaction are negligible in comparison). Therefore, the corresponding Hamiltonian for our problem can be broken up into in-plane and out-of-plane components: $H = H^{\parallel} + H^{\perp}$, where

$$H^{\parallel} = \frac{1}{2} \sum_{i \neq j} \mathbf{S}_i \cdot \mathbf{J}_{ij}^{\parallel} \cdot \mathbf{S}_j + \sum_i \mathbf{S}_i \cdot \mathbf{A}_i \cdot \mathbf{S}_i \quad (1)$$

represents the in-plane exchange (including isotropic and anisotropic coupling) and single-ion terms while

$$H^{\perp} = \frac{1}{2} \sum_{i,j} J_{ij}^{\perp} \mathbf{S}_i \cdot \mathbf{S}_j \quad (2)$$

contains the exchange (isotropic only) between layers¹⁹. Here, $\mathbf{J}_{ij}^{\parallel}$ is the intralayer exchange interaction tensor, J_{ij}^{\perp} is the isotropic interlayer exchange constant, and \mathbf{A}_i is the single-ion anisotropy (SIA) tensor. The intralayer exchange interaction tensor is made up of contributions from isotropic and symmetric anisotropic (also called two-site anisotropy, or TSA) components. The antisymmetric exchange (Dzyaloshinskii–Moriya (DM)) interaction vanishes due to the presence of inversion symmetry^{19,34,35}. The indices i, j denote Ni atom sites wherein we consider up to third nearest neighbor isotropic exchanges both in-plane (Eq. 1) and out-of-plane (Eq. 2) (see Appendix C for schematic representations of these leading interactions). The full tensor has been taken into account for

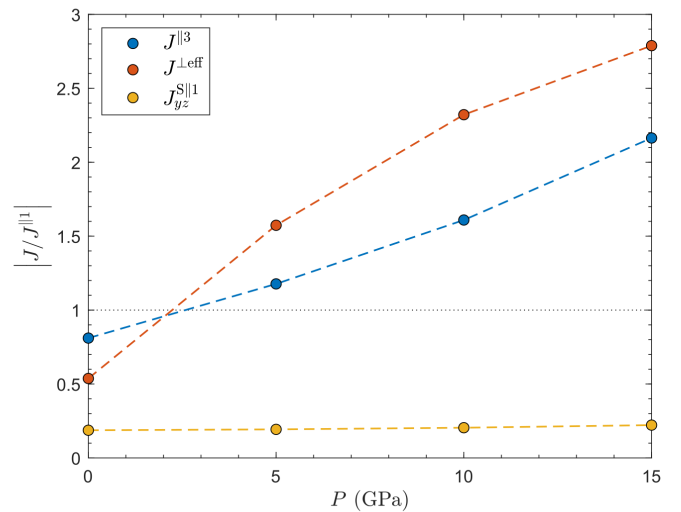


FIG. 4. Ratio of exchange couplings to $J^{\parallel 1}$ at different pressures in bulk Ni₂.

the in-plane nearest neighbor exchange interaction. The single-ion anisotropy in Eq. 1 is an on-site term. The factors of 1/2 in front of the exchange terms account for double-counting. Note the sign conventions in Eqs. 1 and 2 implying that a positive (negative) isotropic exchange interaction favors an antiparallel (parallel) alignment of spins and a positive (negative) scalar single-ion parameter indicates an easy-plane (easy-axis) anisotropy. Further details of the derivation of the magnetic interactions are given in Appendix C.

Table I contains the derived intralayer and interlayer coupling constants for Ni₂ calculated via the four-state method for pressures up to 15 GPa (20 GPa results were not included since at this pressure we obtain a metallic solution). As described before, at ambient pressure the non-collinear magnetic ground state of Ni₂ is realized via the competition between the dominant intralayer FM first-nearest neighbor exchange ($J^{\parallel 1}$) and the AFM third-nearest neighbor exchange ($J^{\parallel 3}$). This competition

Isotropic intralayer exchanges						
P	$J^{\parallel 1}$	$J^{\parallel 2}$	$J^{\parallel 3}$	$J^{\parallel 3}/J^{\parallel 1}$		
0	-4.54	-0.19	+3.68	-0.81		
5	-4.97	-0.30	+5.85	-1.18		
10	-5.04	-0.51	+8.11	-1.61		
15	-4.82	-0.92	+10.43	-2.16		
SIA and intralayer TSA						
P	A	J_{xx}^{SIA}	J_{yy}^{SIA}	J_{zz}^{SIA}	J_{yz}^{SIA}	$J_{yz}^{\text{SIA}}/J^{\parallel 1}$
0	+0.22	-0.62	+0.74	-0.13	-0.85	+0.19
5	+0.26	-0.66	+0.82	-0.16	-0.96	+0.19
10	+0.25	-0.68	+0.89	-0.21	-1.03	+0.20
15	+0.24	-0.65	+0.95	-0.29	-1.07	+0.22
Isotropic interlayer exchanges						
P	$J^{\perp 1}$	$J^{\perp 2}$	$J^{\perp 3}$	$J^{\perp \text{eff}}$	$J^{\perp \text{eff}}/J^{\parallel 1}$	
0	-0.08	+1.48	+0.52	+2.44	-0.54	
5	+0.06	+4.83	+1.47	+7.82	-1.57	
10	+0.35	+7.80	+1.78	+11.70	-2.32	
15	+0.59	+10.55	+1.15	+13.44	-2.79	

TABLE I. Bulk NiI₂ intra- (top panel) and interlayer (bottom panel) isotropic exchange interactions, plus SIA (A), and first-nearest neighbor in-plane TSA constants (middle panel) in the cartesian x, y, z reference where x was chosen to be parallel to the Ni-Ni bonding vector for different pressures (P) calculated via the four-state method. $J^{\perp \text{eff}}$ represents the effective interlayer exchange and is obtained as $J^{\perp 1} + J^{\perp 2} + 2J^{\perp 3}$, where the coefficient in the last term arises because there are twice as many out-of-plane third nearest-neighbors as first- and second nearest-neighbors. Pressure is in units of GPa and exchange values are given in units of meV.

(measured by the ratio $J^{\parallel 3}/J^{\parallel 1} = -0.81$) results in a strong magnetic frustration which favors helimagnetic phases^{19,36}. One other important quantity is the ratio $J_{yz}^{\text{SIA}}/J^{\parallel 1} = 0.19$, that measures the canting of the two-site anisotropy axes from the direction perpendicular to the layers. Finally, the out-of-plane modulation of the magnetic propagation vector in the bulk is determined by a net AFM interlayer exchange $J^{\perp \text{eff}}$ ⁵ which we now decompose further revealing the dominance of the second nearest-neighbor term ($J^{\perp 2}$).

With pressure, the signs of the dominant intralayer isotropic exchange interactions remain: $J^{\parallel 1}$ is FM while $J^{\parallel 3}$ is AFM for all applied pressure values. However, while $J^{\parallel 1}$ is weakly pressure dependent, $J^{\parallel 3}$ significantly increases with pressure, becoming the dominant exchange already at 5 GPa. $J^{\parallel 2}$ remains small in comparison to both $J^{\parallel 1}$ and $J^{\parallel 3}$. As shown in Ref. 24, $J^{\parallel 1}$ and $J^{\parallel 2}$ both comprise two main contributions, one being FM (mostly mediated by $I-p$ states) and the other one AFM (arising mostly from a direct $d-d$ overlap between t_{2g} -like states). Their partial compensation is likely linked to the weak sensitivity of $J^{\parallel 1}$ to pressure. Instead, $J^{\parallel 3}$ only portrays AFM contributions arising from e_g-p hybridizations²⁴, ex-

plaining its monotonic dependence with pressure. In this manner, the $J^{\parallel 3}/J^{\parallel 1}$ ratio changes from -0.81 at ambient pressure to -2.16 at 15 GPa (see Fig. 4). Note that the ratio $|J^{\parallel 3}/J^{\parallel 1}|$ is essential for determining the incommensurate helimagnetic propagation vector^{13,36}. In particular, the observed increase in $|J^{\parallel 3}/J^{\parallel 1}|$ with pressure would favor a shorter in-plane spiral pitch, i.e. a larger in-plane \mathbf{q}_{\parallel} , with larger nearest-neighbor spin angle (see Appendix C). The single-ion (easy-plane) anisotropy and the intralayer anisotropic exchanges do not significantly change with pressure, with the $J_{yz}^{\text{SIA}}/J^{\parallel 1}$ ratio remaining almost constant (and small) up to 15 GPa, as shown in Fig. 4.

Concerning the interlayer exchanges, they increase significantly as a consequence of the large decrease of the c lattice parameter with pressure, as expected in a vdW material. AFM $J^{\perp 2}$ remains the dominant interlayer interaction: at 10 GPa it actually becomes the second-largest interaction overall (behind $J^{\parallel 3}$) and at 15 GPa it even slightly surpasses $J^{\parallel 3}$ to become the dominant exchange interaction. The effective interlayer exchange $J^{\perp \text{eff}}$ also increases monotonically with pressure, as does the magnitude of the ratio $J^{\perp \text{eff}}/J^{\parallel 1}$ (see Fig. 4). The role of the interlayer interaction in stabilizing the helimagnetic transition under pressure can be regarded as a complementary effect to its role in enhancing the transition when going from the monolayer to the bulk⁵.

C. Transition Temperatures

The magnetic constants derived from the four-state method (Table I) along with the optimized structural parameters (Fig. 2) were used in Monte Carlo simulations to obtain the specific heat over a temperature range of 1 to 300 K. For each pressure, the ($T_{N,2}$) temperature was then extracted from the specific heat plots via curve fitting to a general Lorentzian function (see Appendix D). Fig. 5a shows the bulk NiI₂ specific heat vs. temperature plots from ambient pressure up to 15 GPa, where $T_{N,2}$ for each pressure is indicated by a dashed vertical line. $T_{N,2}$ is found to exhibit an almost 3-fold increase between 0 and 10 GPa (from 44 to 128 K), followed by saturation at higher pressure. Fig. 5b shows the $T_{N,2}$ from our MC calculations as a function of pressure, where the data points are normalized with respect to the calculated ambient pressure value ($T_{N,2}(0) = 44.4$ K). The saturation of $T_{N,2}$ above 10 GPa is indicative of the competition between intra- and interlayer interactions (see Appendix E).

MC simulations were also obtained (using the same magnetic parameters and optimized structural data) for mono- and bilayer NiI₂ where it was found that the T_N values as a function of pressure behaved linearly beyond 5 GPa, further supporting the claim that a larger interlayer coupling acts to reduce T_N (see Appendix D). Furthermore, the expected increase in T_N with number of layers was observed.

Overall, our MC simulations indicate that pressure can

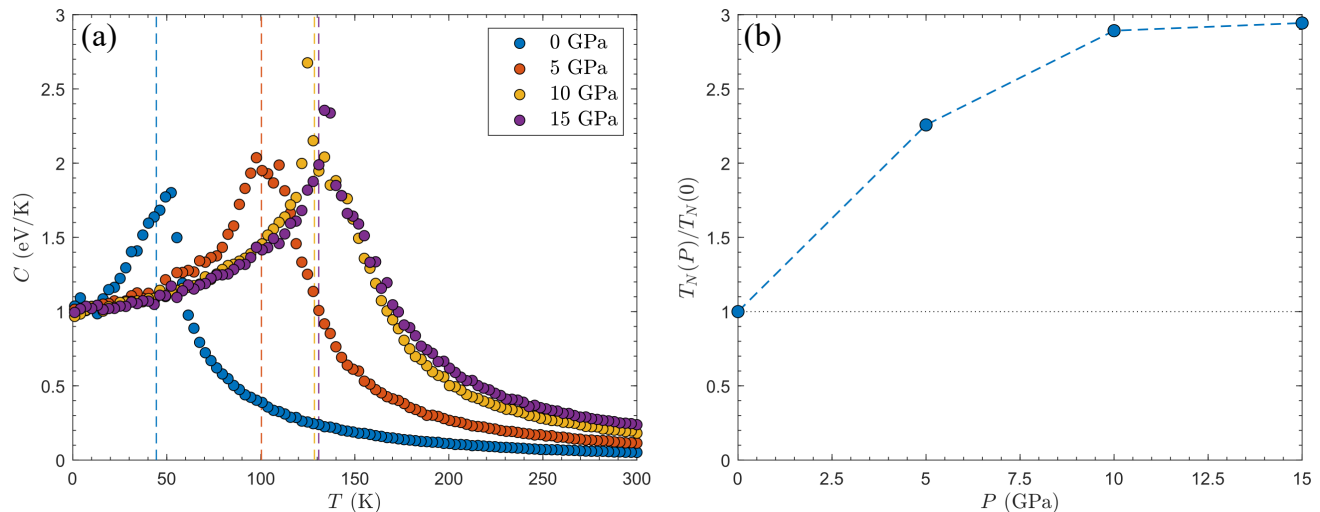


FIG. 5. (a) Bulk NiI_2 specific heat C as a function of temperature T for pressures of 0, 5, 10, and 15 GPa (blue, orange, yellow, and purple circles, respectively) obtained from Monte Carlo simulations. The dashed lines indicate the Néel temperature at each pressure (obtained via curve fitting with a general Lorentzian function): 44.4, 100.3, 128.5, and 130.8 K for 0, 5, 10, and 15 GPa, respectively. (b) Ambient-pressure-normalized Néel temperature values for bulk NiI_2 from MC calculations (blue circles) as a function of pressure P .

be used as a means to enhance the magnetic response of NiI_2 . Even though studies of the induced electric polarization are beyond the scope of our work, we note that the anticipated decrease of the in-plane spiral pitch (as obtained in Appendix C) is expected to enhance the spin-induced polarization (that should be proportional to the relative angle between neighboring spins as long as the spin-polarization tensor is not significantly affected by pressure). As such, pressure could also lead to an enhancement of the multiferroic properties of NiI_2 .

IV. SUMMARY

In this work, we have used first-principles calculations to explore the role of hydrostatic pressure in the structural, electronic, and magnetic response of bulk NiI_2 . DFT-derived structural optimizations show good agreement with XRD data with the experimentally reported insulator-to-metal transition at ~ 19 GPa being correctly reproduced by first-principles simulations. Using the four-state method, we have derived the intralayer and interlayer exchange parameters of NiI_2 (up to third nearest neighbors), finding a helimagnetic ground state with in-plane moments, supported an easy-plane single-ion anisotropy and by the large magnetic frustration between the two dominant in-plane exchange terms ($J^{\parallel 1}$ and $J^{\parallel 3}$) of different sign (ferro- and antiferromagnetic, respectively). The interlayer exchanges are found to be antiferromagnetic

with $J^{\perp 2}$ being dominant. As pressure is increased, $J^{\parallel 3}$ and $J^{\perp 2}$ become the overall dominant interactions with magnitudes that grow monotonically with pressure. This leads to our observation of the calculated bulk Néel temperatures increasing monotonically with pressure up to 10 GPa. They saturate for higher pressures due to the competition between in-plane and out-of-plane couplings. Our results indicate that hydrostatic pressure is a promising way to enhance the magnetic response of NiI_2 and it could likely also be exploited to stabilize its multiferroic state at higher temperatures.

V. ACKNOWLEDGMENTS

We thank S. Picozzi for useful discussions during the early stages of this work. JK and AB acknowledge support from NSF Grant No. DMR 2206987 and the ASU Research Computing Center for high-performance computing resources. DA, BD and MJV acknowledge the SWIPE project funded by FNRS Belgium grant PINT-MULTI R.8013.20. MJV acknowledges ARC project DREAMS (G.A. 21/25-11) funded by Federation Wallonie Bruxelles and ULiege. PB acknowledges financial support from the Italian MIUR through Project No.PRIN 2017Z8TS5B. C.A.O., L.G.P.M., Q.S., and R.C. acknowledge support from the US Department of Energy, BES under Award No. DE-SC0019126 (materials synthesis and characterization and X-ray diffraction measurements).

* jkapeghi@asu.edu

† antia.botana@asu.edu

- ¹ M. Blei, J. L. Lado, Q. Song, D. Dey, O. Erten, V. Pardo, R. Comin, S. Tongay, and A. S. Botana, *Applied Physics Reviews* **8**, 021301 (2021).
- ² X. Wang, K. Du, Y. Y. F. Liu, P. Hu, J. Zhang, Q. Zhang, M. H. S. Owen, X. Lu, C. K. Gan, P. Sengupta, C. Kloc, and Q. Xiong, *2D Materials* **3**, 031009 (2016).
- ³ J.-U. Lee, S. Lee, J. H. Ryoo, S. Kang, T. Y. Kim, P. Kim, C.-H. Park, J.-G. Park, and H. Cheong, *Nano Letters* **16**, 7433 (2016).
- ⁴ B. Huang, G. Clark, E. Navarro-Moratalla, D. R. Klein, R. Cheng, K. L. Seyler, D. Zhong, E. Schmidgall, M. A. McGuire, D. H. Cobden, *et al.*, *Nature* **546**, 270–273 (2017).
- ⁵ Q. Song, C. A. Occhialini, E. Ergeçen, B. Ilyas, D. Amoroso, P. Barone, J. Kapeghian, K. Watanabe, T. Taniguchi, A. S. Botana, S. Picozzi, N. Gedik, and R. Comin, *Nature* **602**, 601 (2022).
- ⁶ J. Nasser, J. Kiat, and R. Gabilly, *Solid State Communications* **82**, 49 (1992).
- ⁷ J. A. A. Ketelaar, *Zeitschrift für Kristallographie - Crystalline Materials* **88**, 26 (1934).
- ⁸ M. A. McGuire, *Crystals* **7** (2017), 10.3390/cryst7050121.
- ⁹ A. Adam, D. Billerey, C. Terrier, R. Mainard, L. Regnault, J. Rossat-Mignod, and P. Mériel, *Solid State Communications* **35**, 1 (1980).
- ¹⁰ P. Day, A. Dinsdale, E. R. Krausz, and D. J. Robbins, *Journal of Physics C: Solid State Physics* **9**, 2481 (1976).
- ¹¹ P. Day and K. R. A. Ziebeck, *Journal of Physics C: Solid State Physics* **13**, L523 (1980).
- ¹² D. Billerey, C. Terrier, N. Ciret, and J. Kleinclauss, *Physics Letters A* **61**, 138 (1977).
- ¹³ S. Kuindersma, J. Sanchez, and C. Haas, *Physica B+C* **111**, 231 (1981).
- ¹⁴ H. Liu, X. Wang, J. Wu, Y. Chen, J. Wan, R. Wen, J. Yang, Y. Liu, Z. Song, and L. Xie, *ACS Nano* **14**, 10544 (2020).
- ¹⁵ T. Kurumaji, S. Seki, S. Ishiwata, H. Murakawa, Y. Kaneko, and Y. Tokura, *Phys. Rev. B* **87**, 014429 (2013).
- ¹⁶ G. Kresse and D. Joubert, *Phys. Rev. B* **59**, 1758 (1999).
- ¹⁷ G. Kresse and J. Furthmüller, *Phys. Rev. B* **54**, 11169 (1996).
- ¹⁸ G. Kresse and J. Furthmüller, *Computational Materials Science* **6**, 15 (1996).
- ¹⁹ D. Amoroso, P. Barone, and S. Picozzi, *Nat Commun* **11**, 5784 (2020).
- ²⁰ J. P. Perdew, K. Burke, and M. Ernzerhof, *Phys. Rev. Lett.* **77**, 3865 (1996).
- ²¹ S. Grimme, J. Antony, S. Ehrlich, and H. Krieg, *The Journal of Chemical Physics* **132**, 154104 (2010).
- ²² A. I. Liechtenstein, V. I. Anisimov, and J. Zaanen, *Phys. Rev. B* **52**, R5467 (1995).
- ²³ A. Rohrbach, J. Hafner, and G. Kresse, *Journal of Physics: Condensed Matter* **15**, 979 (2003).
- ²⁴ K. Riedl, D. Amoroso, S. Backes, A. Razpopov, T. P. T. Nguyen, K. Yamauchi, P. Barone, S. M. Winter, S. Picozzi, and R. Valentí, *Phys. Rev. B* **106**, 035156 (2022).
- ²⁵ H. Xiang, C. Lee, H.-J. Koo, X. Gong, and M.-H. Whangbo, *Dalton Trans.* **42**, 823 (2013).
- ²⁶ H. J. Xiang, E. J. Kan, S.-H. Wei, M.-H. Whangbo, and X. G. Gong, *Phys. Rev. B* **84**, 224429 (2011).
- ²⁷ D. Šabani, C. Bacaksiz, and M. V. Milošević, *Phys. Rev. B* **102**, 014457 (2020).
- ²⁸ C. Xu, J. Feng, H. Xiang, and L. Bellaiche, *npj Computational Materials* **4** (2018), 10.1038/s41524-018-0115-6.
- ²⁹ C. Xu, J. Feng, S. Prokhorenko, Y. Nahas, H. Xiang, and L. Bellaiche, *Phys. Rev. B* **101**, 060404 (2020).
- ³⁰ B. D. et al., “github.com/bertdupe/matjes,”.
- ³¹ S. Hayami, S.-Z. Lin, and C. D. Batista, *Phys. Rev. B* **93**, 184413 (2016).
- ³² C. D. Batista, S.-Z. Lin, S. Hayami, and Y. Kamiya, *Reports on Progress in Physics* **79**, 084504 (2016).
- ³³ M. P. Pasternak, G. Hearne, E. Sterer, R. D. Taylor, and R. Jeanloz, *AIP Conference Proceedings* **309**, 335 (1994).
- ³⁴ T. Moriya, *Phys. Rev.* **120**, 91 (1960).
- ³⁵ E. Simon, K. Palotás, B. Ujfalussy, A. Deák, G. Stocks, and L. Szunyogh, *Journal of Physics: Condensed Matter* **26**, 186001 (2014).
- ³⁶ E. Rastelli, A. Tassi, and L. Reatto, *Physica B+C* **97**, 1 (1979).
- ³⁷ J. Klimeš, D. R. Bowler, and A. Michaelides, *Phys. Rev. B* **83**, 195131 (2011).
- ³⁸ G. J. Vida, E. Simon, L. Rózsa, K. Palotás, and L. Szunyogh, *Phys. Rev. B* **94**, 214422 (2016).

Appendix A: XRD Data and Extended Structural Parameter Calculations

High-pressure XRD measurements were performed at Sector 16-ID-B at the Advanced Photon Source, Argonne National Laboratory using an incident energy of $E = 29.2$ keV. High-quality powder samples of NiI_2 grown by chemical vapor transport⁵ were loaded into a custom double-sided membrane-driven diamond anvil cell using Neon as a pressure transmitting medium with pressure monitored in-situ by ruby fluorescence. The results of the XRD measurements done at 200 K over a pressure range of ~ 1 to ~ 20 GPa are shown in Fig. 6. In-plane lattice parameter values can be extracted from either the $10\bar{2}$ or $2\bar{1}0$ peaks at each pressure (both of which undergo splitting above ~ 15 GPa, indicative of the rhombohedral to monoclinic phase transition), while out-of-plane lattice parameters can be obtained from the 0012 peaks. In-plane and out-of-plane lattice parameter values from the XRD measurements are given in Tables II and III, respectively.

In order to obtain the best agreement with the XRD lattice parameters, three Hubbard U values (0, 3.24, and 5.8 eV), along with two exchange-correlation functionals were tested in the DFT calculations. The chosen test functionals were (i) a PBE exchange-correlation functional²⁰ with added DFT-D3 vdW correction²¹ and (ii) a semilocal optB86b exchange-correlation functional³⁷ augmented with a nonlocal PBE correlation functional. Tables II and III contain the 0 to 20 GPa results of the optimized in-plane and out-of-plane lattice parameters, respectively, for the bulk NiI_2 system in an AFM spin configuration. As can be seen in Table II, for a particular pressure and U value, the in-plane lattice parameters are not significantly affected by the choice of DFT functional. On the other hand, increasing U gives rise to an increase in the lattice parameters. From Table III, it is clear that the out-of-plane lattice parameter is, as expected, more sensitive to the choice of functional. Based on structural data alone, one would conclude that the PBE+D3 functional with a U of 5.8 eV gives rise to the best agreement with experimental data. However, at this U value the bulk system would still be insulating at 20 GPa, inconsistent with the known bulk insulator-to-metal transition at 19 GPa³³. Thus, we proceed to use in the main text the structural data obtained for relaxations with PBE+D3 and $U = 3.24$ eV, which still provide relatively good agreement with experimental lattice parameters, and also reproduce the experimentally observed insulator-to-metal transition with pressure.

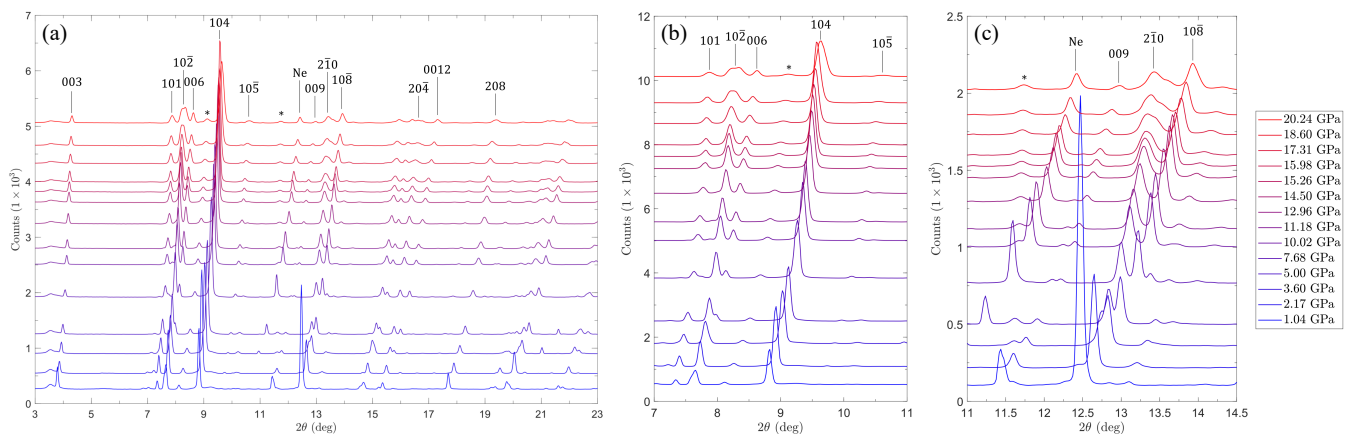


FIG. 6. (a) Bulk XRD spectrum at 200 K for increasing pressure (from ~ 1 GPa in blue to ~ 20 GPa in red). (b) and (c) show zoomed-in sections of the spectrum to highlight the splitting in the $10\bar{2}$ and $2\bar{1}0$ peaks, respectively, above ~ 15 GPa.

P (GPa)	DFT: optB86b			DFT: PBE+D3			XRD
	$U = 0.00$	$U = 3.24$	$U = 5.80$	$U = 0.00$	$U = 3.24$	$U = 5.80$	
0	3.91	3.93	3.95	3.93	3.95	3.97	-
5	3.79	3.81	3.82	3.81	3.82	3.84	3.80
10	3.70	3.73	3.73	3.67	3.73	3.74	3.72
15	3.62	3.66	3.66	3.61	3.67	3.67	3.66
20	3.56	3.61	3.61	3.56	3.61	3.61	3.63/3.59

TABLE II. In-plane lattice parameters $a = b$ (in units of Å) for bulk NiI₂ from DFT optimization calculations (using an AFM spin configuration) and XRD measurements at pressures (P) of 0 to 20 GPa. DFT results are shown for two functionals, optB86b and PBE+D3, for which three Hubbard U values were tested: 0, 3.24, and 5.8 eV (with corresponding Hund's J_H values of 0, 0.68, and 0.8 eV, respectively). XRD results are given for measurements taken at 200 K. As mentioned in the main text, above ~ 15 GPa there is a phase transition to monoclinic symmetry so both values for the in-plane lattice constant are provided for the 20 GPa case.

P (GPa)	DFT: optB86b			DFT: PBE+D3			XRD
	$U = 0.00$	$U = 3.24$	$U = 5.80$	$U = 0.00$	$U = 3.24$	$U = 5.80$	
0	18.83	19.44	19.69	19.07	19.72	19.99	-
5	17.60	18.08	18.35	17.56	18.11	18.41	18.31
10	17.07	17.50	17.77	16.94	17.45	17.76	17.69
15	16.74	17.10	17.39	16.64	17.03	17.35	17.31
20	16.52	16.78	17.10	16.39	16.66	17.04	16.92

TABLE III. Out-of-plane lattice parameters c (in units of Å) for bulk NiI₂ from DFT optimization calculations (using an AFM spin configuration) and XRD measurements at pressures (P) of 0 to 20 GPa. DFT results are shown for two functionals, optB86b and PBE+D3, for which three Hubbard U values were tested: 0, 3.24, and 5.8 eV (with corresponding Hund's J_H values of 0, 0.68, and 0.8 eV, respectively). XRD results are given for measurements taken at 200 K.

Appendix B: Comparison between Bulk and Bilayer and Extended Band Structure Calculations

P (GPa)	Bilayer			Bulk		
	ΔE (meV)	$J^{\perp\text{eff}}$ (meV)	$E_{\text{gap}}^{\text{AFM}}$ (eV)	ΔE (meV)	$J^{\perp\text{eff}}$ (meV)	$E_{\text{gap}}^{\text{AFM}}$ (eV)
0	6.8	2.3	0.99	13.6	2.3	0.98
5	23.7	7.9	0.75	47.3	7.9	0.70
10	41.1	13.7	0.54	81.5	13.6	0.40
15	59.2	19.7	0.33	105.4	17.6	0.14
20	74.4	24.8	0.14	108.7	18.1	0.00

TABLE IV. Energy difference between FM and AFM states (ΔE) along with the corresponding effective interlayer exchange ($J^{\perp\text{eff}}$) for bilayer and bulk NiI₂ at pressures (P) of 0 to 20 GPa. AFM band gap energies ($E_{\text{gap}}^{\text{AFM}}$) for bilayer and bulk NiI₂ are also given.

Table IV shows the energy difference (per formula unit) between the FM and AFM spin configurations for bilayer and bulk NiI₂: $\Delta E = E_{\text{FM}} - E_{\text{AFM}}$. A simple Heisenberg Hamiltonian $H = (J^{\perp\text{eff}}/2) \sum_{i,j} \mathbf{S}_i \cdot \mathbf{S}_j$ captures the effective interlayer exchange interaction, where $J^{\perp\text{eff}}$ is the isotropic exchange constant between spins $\mathbf{S}_{i,j}$ on out-of-plane first-nearest neighbor Ni lattice sites i, j . Again, the factor of 1/2 in front of the summation is to account for double-counting. In the bilayer (bulk) case there are 3 (6) nearest out-of-plane neighbors, and so we obtain the following energy equations for the two spin states: $E_{\text{FM}}^{\text{bilayer}} = E_0 + (3/2)J^{\perp\text{eff}}S^2$ ($E_{\text{FM}}^{\text{bulk}} = E_0 + 3J^{\perp\text{eff}}S^2$) and $E_{\text{AFM}}^{\text{bilayer}} = E_0 - (3/2)J^{\perp\text{eff}}S^2$ ($E_{\text{AFM}}^{\text{bulk}} = E_0 - 3J^{\perp\text{eff}}S^2$), where E_0 is the total energy for the system omitting magnetic interactions and note that $S^2 = |\mathbf{S}|^2$. Taking the difference yields $\Delta E^{\text{bilayer}} = E_{\text{FM}}^{\text{bilayer}} - E_{\text{AFM}}^{\text{bilayer}} = 3J^{\perp\text{eff}}S^2$

and $\Delta E^{\text{bulk}} = E_{\text{FM}}^{\text{bulk}} - E_{\text{AFM}}^{\text{bulk}} = 6J^{\perp\text{eff}}S^2$. Finally, solving for the interlayer exchange in each case, we have $J^{\perp\text{eff}} = (E_{\text{FM}}^{\text{bilayer}} - E_{\text{AFM}}^{\text{bilayer}})/3S^2$ and $J^{\perp\text{eff}} = (E_{\text{FM}}^{\text{bulk}} - E_{\text{AFM}}^{\text{bulk}})/6S^2$. With $S_{\text{Ni}} = 1$, we obtain the bilayer and bulk $J^{\perp\text{eff}}$ values given in Table IV, where at each pressure $\Delta E > 0$ indicating that the ground state is AFM for both systems. Subsequently, $J^{\perp\text{eff}} > 0$ indicating an AFM exchange. Further, note that the exchange is nearly identical in both systems up to 10 GPa, after which the bilayer exchange becomes larger than in the bulk. In both systems, however, we see a trend of monotonically increasing exchange with pressure, as one would expect considering the decreasing interlayer distance.

Table IV also shows the evolution with pressure of the band gap energies for bulk and bilayer NiI_2 for an AFM state (consisting of ferromagnetic planes coupled antiferromagnetically out-of-plane). The corresponding electronic band structures are shown in Fig. 7 (the first BZ is illustrated in Fig. 7a where the chosen k -path is indicated). A decrease in the band gap with increasing pressure can be observed along with an increase in the bandwidths. This is expected since the out-of-plane lattice parameter, and thus the interlayer distance, decreases as pressure increases. In the bilayer case, the system remains insulating up to 20 GPa, while the bulk transitions to a metal between 15 and 20 GPa, consistent with the known insulator-to-metal transition of 19 GPa. In the bilayer band structures, flat bands between Γ and A at each pressure can be observed as well as nearly identical $k_z = 0$ and $k_z = 0.5$ band structures, implying that the bilayer is indeed isolated. In contrast, significantly dispersive bands can be observed in the bulk between Γ and A (with the dispersion increasing with pressure), and also there is clear variation between the $k_z = 0$ and $k_z = 0.5$ band structures.

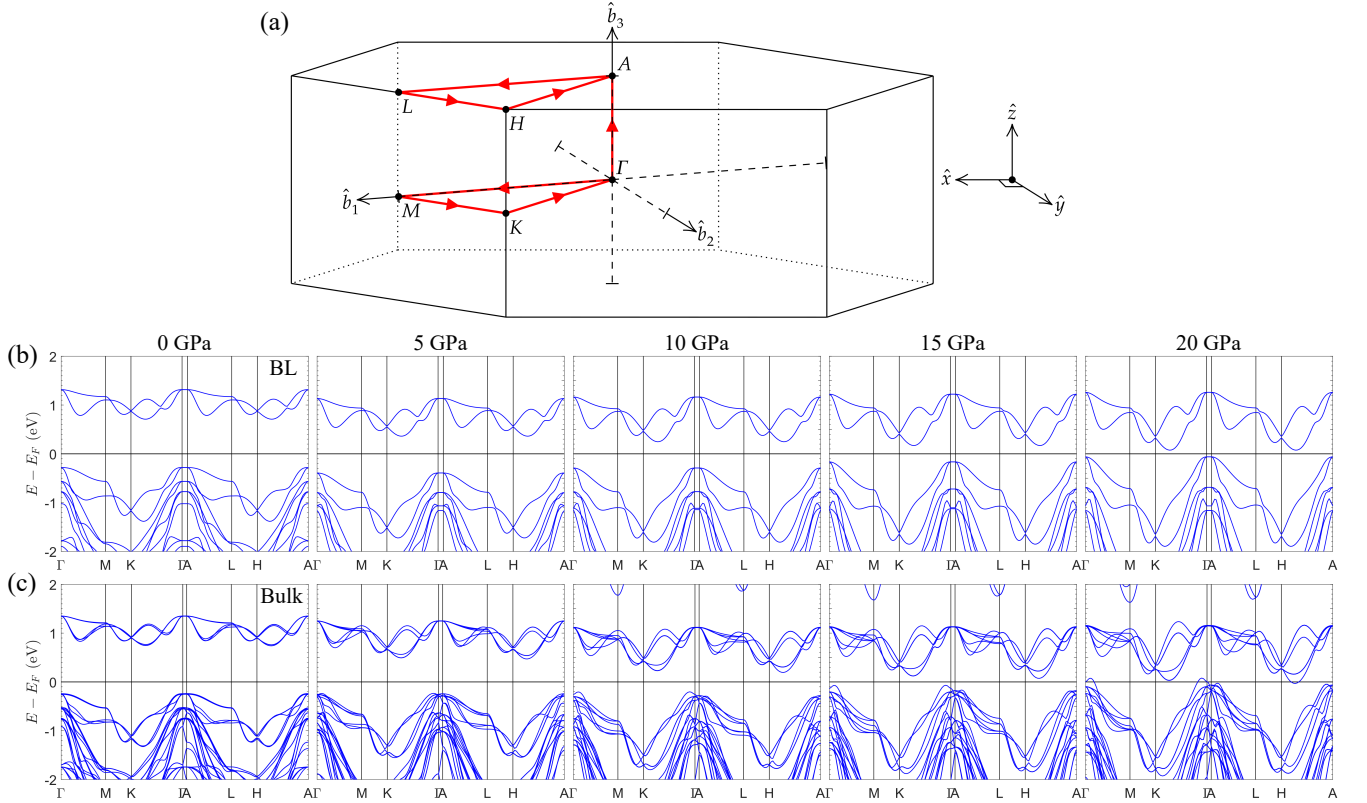


FIG. 7. (a) First Brillouin zone for NiI_2 where high-symmetry points are labeled and the chosen k -path for our electronic structure calculations is indicated by the red arrows. The high symmetry points correspond to: $\Gamma = (0, 0, 0)$, $M = (1/2, 0, 0)$, $K = (1/3, 1/3, 0)$, $A = (0, 0, 1/2)$, $L = (1/2, 0, 1/2)$, $H = (1/3, 1/3, 1/2)$. (b) Electronic structure for bilayer NiI_2 in an AFM spin configuration from 0-20 GPa. (c) Electronic structure for bulk NiI_2 in an AFM spin configuration from 0-20 GPa.

To determine the orbital character of these dispersive bands, we look at the orbital-resolved density of states (DOS) and also the band character plots for bulk NiI_2 as shown in Fig. 8. The I - p states at 0 and 15 GPa are shown in Figs. 8a and 8b, respectively, while the Ni- d states are shown in Figs. 8c and 8d, respectively. The I - p states lie directly below the Fermi level and have partial hybridization with the Ni- d states which are lower in energy. Clearly, the highly dispersive bands between Γ and A come mostly from the I - p_z states, but they have Ni- d_{z^2} admixture as well.

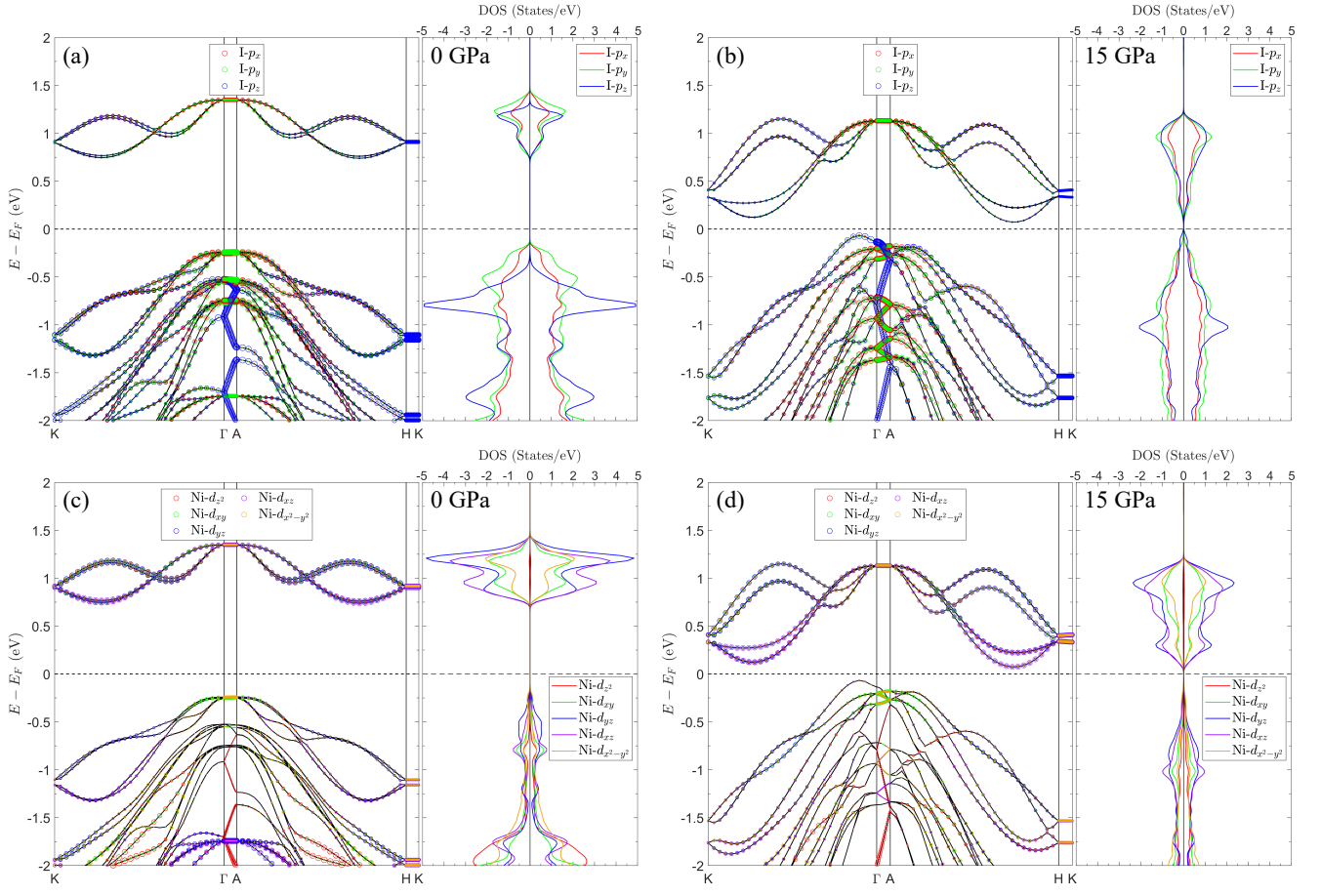


FIG. 8. Band character plots and orbital-resolved density of states for AFM bulk Ni₂. (a) I-*p* states at 0 GPa. (b) I-*p* states at 15 GPa. (c) Ni-*d* states at 0 GPa. (d) Ni-*d* states at 15 GPa. Note that here we use a different k-path than in the previous electronic structures in Fig. 7 to better show the band dispersion from Γ to A.

Appendix C: Further Details on the Exchange Interactions

The exchange interaction tensor can be decomposed into contributions from isotropic as well as anisotropic exchanges. The isotropic component is given by $J_{ij}^{\parallel} = \frac{1}{3} \text{Tr} [\mathbf{J}_{ij}^{\parallel}]$, where Tr is the trace operator over spatial directions. The anisotropic contributions can be further decomposed into antisymmetric and symmetric components, ($\mathbf{J}_{ij}^{\text{A}\parallel}$ and $\mathbf{J}_{ij}^{\text{S}\parallel}$, respectively), the effects of which will tend to favor either an alignment of the spins in a given direction, as in the symmetric case, or a canting of spin pairs, as in the antisymmetric case. The antisymmetric exchange corresponds to the Dzyaloshinskii–Moriya (DM) interaction, which is zero for an inversion center at the point bisecting the Ni-Ni bond, as in the present case^{19,34,35,38}. The symmetric exchange (two-site anisotropy) on the other hand, has the form $\mathbf{J}_{ij}^{\text{S}\parallel} = \frac{1}{2} \left(\mathbf{J}_{ij}^{\parallel} + [\mathbf{J}_{ij}^{\parallel}]^{\text{T}} \right) - J_{ij}^{\parallel} \mathbf{I}$ (here \mathbf{I} is the unit matrix and the superscript T denotes the transpose) and can play an important role in the spontaneous stabilization of noncollinear magnetic states¹⁹. For a Ni-Ni pair whose bond is along the Cartesian \hat{x} axis, the exchange tensor has the form¹⁹

$$\mathbf{J}^{\parallel} = \begin{pmatrix} J_{xx}^{\parallel} & 0 & 0 \\ 0 & J_{yy}^{\parallel} & J_{yz}^{\parallel} \\ 0 & J_{zy}^{\parallel} & J_{zz}^{\parallel} \end{pmatrix}.$$

Note that, by symmetry, $J_{yz}^{\parallel} = J_{zy}^{\parallel}$ and the other off-diagonal terms are zero in the absence of DMI. Lastly, the SIA tensor in Eq. 1 can be simplified due to the local symmetry of Ni ions which has the Cartesian \hat{z} -direction parallel with the crystallographic *c* axis, hence $H^{\text{SIA}} = \sum_i A_i (S_{i,z})^2$, where A_i is now a scalar¹⁹.

In Fig. 9 we show the intra- and interlayer nearest neighbors for mono- and bilayer NiI_2 lattices. In each system, the nearest neighbor Ni atom pairs chosen for the four-state calculations are indicated. In the monolayer, the $\text{Ni}_0 - \text{Ni}_1^{\parallel}$ pair is chosen for the first nearest neighbor interaction ($J^{\parallel 1}$), the $\text{Ni}_0 - \text{Ni}_2^{\parallel}$ pair is chosen for the second nearest neighbor interaction ($J^{\parallel 2}$), and the $\text{Ni}_0 - \text{Ni}_3^{\parallel}$ pair is chosen for the third nearest neighbor interaction ($J^{\parallel 3}$). In the bilayer, the $\text{Ni}_0 - \text{Ni}_1^{\perp}$ pair is chosen for the first nearest neighbor interaction ($J^{\perp 1}$), the $\text{Ni}_0 - \text{Ni}_2^{\perp}$ pair is chosen for the second nearest neighbor interaction ($J^{\perp 2}$), and the $\text{Ni}_0 - \text{Ni}_3^{\perp}$ pair is chosen for the third nearest neighbor interaction ($J^{\perp 3}$).

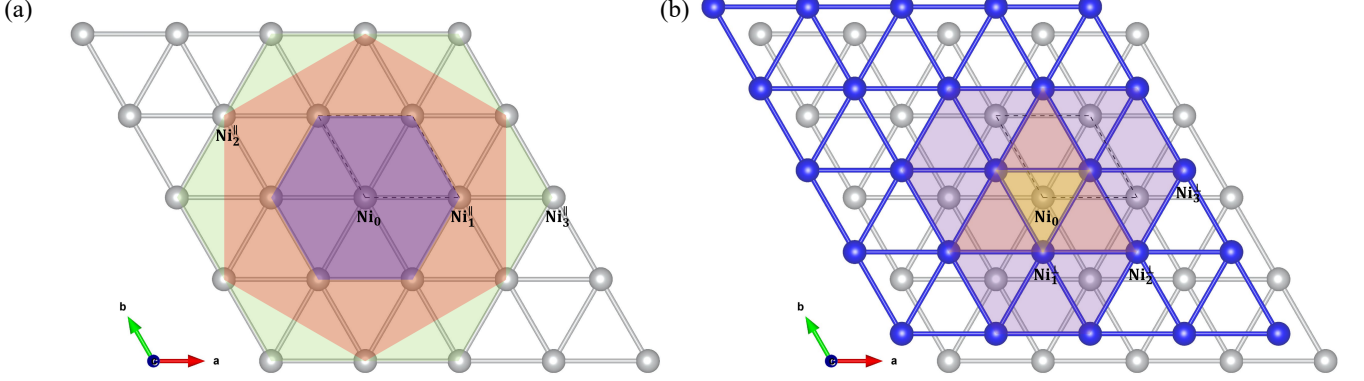


FIG. 9. (a) Triangular lattice of Ni atoms (gray spheres) in monolayer NiI_2 illustrating intralayer nearest neighbors. Ni_0 is the central atom and the Ni atoms at the corners of the blue, red, and green hexagons are the first, second, and third in-plane nearest neighbors of Ni_0 , respectively. (b) Triangular lattice of Ni atoms (gray spheres in the bottom layer and blue spheres in the top layer) in bilayer NiI_2 illustrating the interlayer nearest neighbors. Ni_0 is the central atom and the Ni atoms at the corners of the yellow and orange triangles are the first and second out-of-plane nearest neighbors of Ni_0 , respectively, while the atoms at the corners of the purple polygon are the third out-of-plane nearest neighbors of Ni_0 . In (a) and (b) the unit cells are indicated by black dashed lines.

Table V contains the ratio of $J^{\parallel 1}$ and $J^{\parallel 3}$ from the four-state calculations, which is used to obtain the magnetic propagation vector $q = |\mathbf{q}| = 2 \arccos \left[\left(1 + \sqrt{1 - 2(J^{\parallel 1}/J^{\parallel 3})} \right) / 4 \right]$ ^{31,32}. This can then be used to obtain the size of the magnetic unit cell $L_{\text{m.u.c.}} \sim 4\pi/q$. A decrease in the $J^{\parallel 1}/J^{\parallel 3}$ ratio with pressure leads to an increase in q , which results in a shorter pitch of the in-plane spin-spiral and consequently a smaller magnetic unit cell length $L_{\text{m.u.c.}}$.

P (GPa)	$J^{\parallel 1}/J^{\parallel 3}$	q	$L_{\text{m.u.c.}}$
0	-1.23	0.12	8.12
5	-0.85	0.14	7.40
10	-0.62	0.14	7.01
15	-0.46	0.15	6.75
20	-0.36	0.15	6.58

TABLE V. Ratio of leading intralayer exchanges $J^{\parallel 1}/J^{\parallel 3}$ in bulk NiI_2 at pressures P up to 20 GPa with the corresponding magnetic propagation vector magnitude q and magnetic unit cell length $L_{\text{m.u.c.}}$.

Appendix D: Extended MC calculations

In Fig. 10 we show the specific heat calculated from MC as a function of temperature for the mono- and bilayer NiI_2 systems as a function of pressure (up to 15 GPa). The Néel temperature at each pressure was obtained by fitting the specific heat vs. temperature plot using a general Lorentzian curve of the form $C(T) = f(x) = C_0 + \frac{2A}{\pi} \left(\frac{w}{w^2 + 4(x - x_c)^2} \right)$, where A is the area under the curve, w is the width of the peak, x_c is the peak maximum, C_0 is the offset, and $[A, w, x_c, C_0] \in \mathbb{R}$. Here, the Néel temperature T_N is equal to x_c . The particular Néel temperature values for monolayer, bilayer, and bulk NiI_2 from 0-15 GPa are given in Table VI and also plotted vs. pressure in Fig. 10c. In mono- and bilayers, T_N increases monotonically with pressure but a monotonic increase in T_N with layer number can also be observed, which is consistent with the literature⁵. The mono- and bilayer ambient pressure T_N values themselves are

consistent with the literature with a Néel temperature of 21 K and 30 K reported for monolayer and bilayer NiI₂, respectively⁵. While both mono- and bilayer Néel temperatures increase linearly with pressure up to 15 GPa (with slopes of 2.4 and 2.0 K/GPa, respectively) the bulk values appear to saturate around ~130 K above 10 GPa, the cause of which is examined in Appendix E.

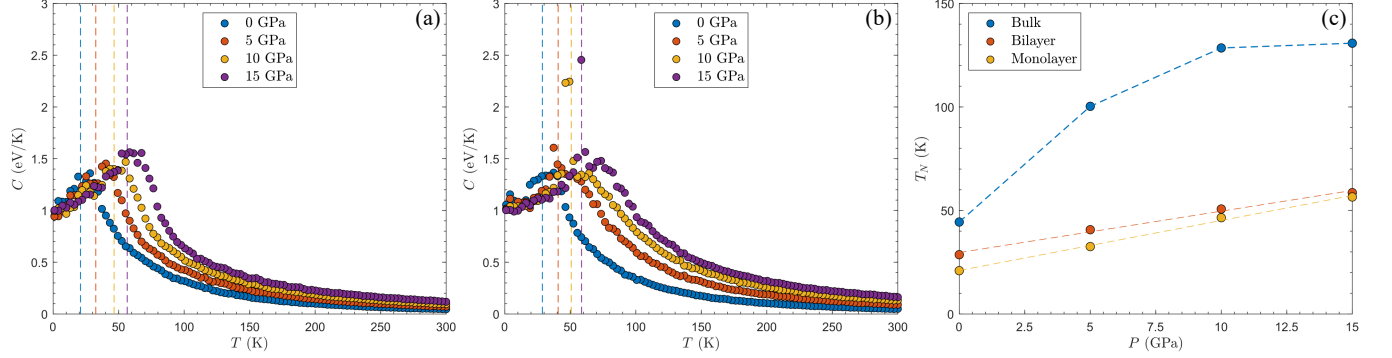


FIG. 10. (a) Monolayer and (b) bilayer NiI₂ specific heat C as a function of temperature T for pressures of 0, 5, 10, and 15 GPa (blue, orange, yellow, and purple circles, respectively) obtained from Monte Carlo simulations. The dashed lines indicate the Néel temperature at each pressure (obtained via curve fitting with a general Lorentzian function). (c) Néel temperature values for bulk, bilayer, and monolayer NiI₂ from MC calculations (blue, orange, and yellow circles, respectively) as a function of pressure P . The dashed lines represent linear best-fits to the MC data (except in the bulk case where the dashed line simply connects the data points to serve as a guide for the eye).

P (GPa)	T_N^{ML} (K)	T_N^{BL} (K)	T_N^{Bulk} (K)
0	20.9	28.7	44.4
5	32.6	40.7	100.3
10	46.5	50.7	128.5
15	56.5	58.6	130.8

TABLE VI. Néel temperatures (T_N) for monolayer (ML), bilayer (BL), and bulk NiI₂ systems from MC calculations at pressures (P) of 0 to 15 GPa.

Appendix E: Mean-Field Approach to NiI₂ Critical Temperature Under Pressure

To further investigate the saturation of T_N above 10 GPa, we estimate the Néel temperature of NiI₂ at different pressures from a mean-field standpoint. First, we derive the mean-field estimate for T_N assuming a simple AFM configuration of FM layers coupled antiferromagnetically. For the sake of simplicity, we consider a minimal Heisenberg model with only isotropic $J^{\parallel 1}$, $J^{\parallel 3}$, and an effective interlayer coupling $J^{\perp \text{eff}}$. In a mean-field approach, one has to derive an effective Weiss field B_i , generated from neighboring spins, acting on a target spin S_i . For classical spins, the expectation value of the local magnetization is then derived from

$$M_i = \langle S_i \rangle = \coth(\beta B_i) - \frac{1}{\beta B_i} \approx \frac{\beta B_i}{3}, \quad (\text{E1})$$

where $\beta = 1/k_B T$ with T being the temperature and k_B the Boltzmann constant. The last approximated equality is valid in the limit of vanishing Weiss field, i.e. close to the transition of the sought ordered phase. As the Weiss field depends on the magnetization, Eq. E1 represents a self-consistent equation for the critical temperature.

In the simple AFM configuration, we can distinguish two magnetic sub-lattices M_1 and M_2 , each defined in alternating layers (e.g., M_1 in odd layers and M_2 in even ones). Then, the AFM order parameter is defined simply as $L = M_1 - M_2$, while the FM order parameter is $M_1 + M_2$. Taking into account the rhombohedral structure of NiI₂, the Weiss fields are thus

$$\begin{aligned} B_1 &= -J_{\parallel} M_1 - J_{\perp} M_2, \\ B_2 &= -J_{\parallel} M_2 - J_{\perp} M_1, \end{aligned} \quad (\text{E2})$$

where $J_{\parallel} = 6J^{\parallel 1} + 6J^{\parallel 3}$ and $J_{\perp} = 6J^{\perp \text{eff}}$. Combining Eqs. E1 and E2 and using the definition of order parameters, the following expressions are obtained:

$$M = -\frac{\beta}{3} (J_{\parallel} + J_{\perp}) M, \quad (\text{E3a})$$

$$L = -\frac{\beta}{3} (J_{\parallel} - J_{\perp}) L. \quad (\text{E3b})$$

Using the last equation, the mean-field estimate for the AFM critical temperature is thus $3k_B T_c = J_{\perp} - J_{\parallel}$ (note that it is positive, as negative/positive exchange constants denote FM/AFM interactions).

The critical temperature for the helimagnetic configuration can be similarly deduced, imposing that the spins surrounding the targeted one (for which we want to identify the Weiss field) are arranged according to the magnetic propagation vector. We assume the in-plane propagation vector with the value of q that minimizes the classical energy, i.e. $q = 2 \arccos \left[\left(1 + \sqrt{1 - 2(J^{\parallel 1}/J^{\parallel 3})} \right) / 4 \right]$. Now the Weiss fields can still be formally written as in Eq. E2, simply replacing

$$\begin{aligned} J_{\parallel} &\mapsto J_{\parallel}(q) = 4J^{\parallel 1} \cos\left(\frac{q}{2}\right) + (2J^{\parallel 1} + 4J^{\parallel 3}) \cos(q) + 2J^{\parallel 3} \cos(2q), \\ J_{\perp} &\mapsto J_{\perp}(q) = 2J^{\perp \text{eff}} (1 + \cos(q) + \cos(2q)). \end{aligned} \quad (\text{E4})$$

It follows that the mean-field estimate for the helimagnetic configuration with AFM modulation along the c axis is formally given by Eq. E3b upon replacements of Eqs. E4, that is

$$3k_B T_c = J_{\perp}(q) - J_{\parallel}(q). \quad (\text{E5})$$

Despite the severe approximations introduced by i) the mean-field Weiss approach and ii) simplifying the model to only three interactions (including an effective interlayer one) and also neglecting anisotropies, the mean-field prediction works surprisingly well, and most importantly it reproduces the saturation behaviour under pressure, as shown in Fig. 11a. This stems from the interplay of interlayer and intralayer terms, with the strongest effect seeming to come from $J_{\perp}(q)$ (which is a function not only of $J^{\perp \text{eff}}$, but $J^{\parallel 1}$ and $J^{\parallel 3}$ as well), as the optimal q depends explicitly on the Heisenberg exchange interactions also. Therefore, the saturation seems to arise from a competition between all interactions, and not merely between the dominant $J^{\perp \text{eff}}$ and $J^{\parallel 3}$.

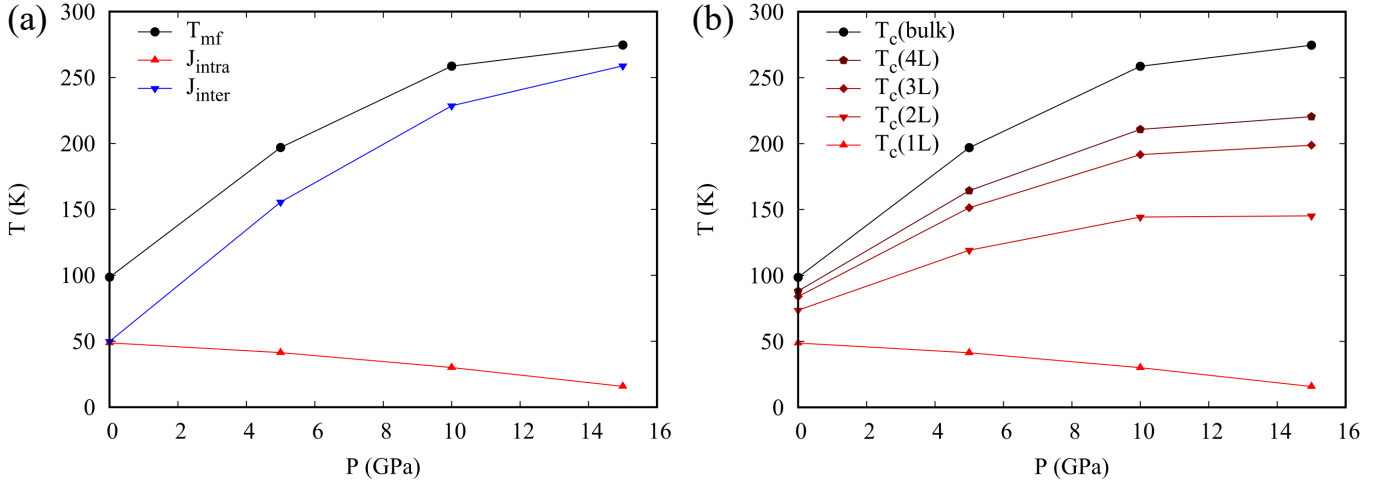


FIG. 11. (a) Evolution of the mean-field (mf) estimate of T_c under pressure using the exchange parameters $J^{\perp \text{eff}}$, $J^{\parallel 1}$, and $J^{\parallel 3}$ taken from Table I in the main text. The labels J_{intra} and J_{inter} denote the intralayer $-J_{\parallel}(q)$ and interlayer $J_{\perp}(q)$ contributions to T_{mf} , respectively. (b) Evolution of mean-field estimate of T_c under pressure for different number of layers, from the monolayer (intralayer contribution only) to 4 layers, with same parameters used in (a). The prediction for the bulk T_c is also shown as a reference.

Although the mean-field approach largely overestimates T_c , a well-known consequence of neglecting fluctuations (in this case it may also come from the simplified model, where we neglected $J^{\parallel 2}$ as well as the real topology of interlayer couplings $J^{\perp 1}$, $J^{\perp 2}$, and $J^{\perp 3}$), the order of magnitude of the pressure-induced enhancement of T_c is consistent with

the MC simulations shown in Fig. 5 (i.e. roughly a three-fold increase at the largest considered pressure). On the other hand, the intralayer contribution to T_c is found to decrease in this mean-field approach, which is inconsistent with the MC results (the inclusion of the second-nearest neighbor interaction partly corrects the trend).

Lastly, one can in principle adopt the same mean-field scheme to address the dependence on the number of layers. The mean-field formulas are consistent with previous MC calculations in showing that

$$\frac{T_c^{\text{bulk}}}{T_c^{\text{1L}}} = 1 + \frac{J_{\perp}(q)}{J_{\parallel}(q)} = 1 + \frac{J^{\perp\text{eff}}}{J^{\parallel 1}} \rho \left(q, \frac{J^{\parallel 3}}{J^{\parallel 1}} \right). \quad (\text{E6})$$

The mean-field temperatures for $L = 2, 3, 4$ were also calculated, but in these cases the expression for a general L can not be extrapolated as one has to find an iterative solution for the self-consistent Weiss equations. Trends in T_c for $L = 2, 3, 4$ are shown in Fig. 11b and are roughly consistent with expectations but with same issues discussed previously.